Incompressible Laminar Navier-Stokes

Mohammad ZANDSALIMY

December 20, 2021

Problem

The 2 dimensional incompressible, laminar, Navier-Stokes equations are solved on a regular Cartesian numerical grid. The problem is the famous lid driven square cavity at different mesh size and Reynolds numbers. Space discretization is second order accurate and implicit Euler method of time advancing is utilized for integration in time. Artificial compressibility method is used to couple the momentum equations and the continuity equation. These equations can be written in matrix form as Eq. 1 with the solution and flux vectors as in Eq. 2. In all of my simulations, the convergence criteria is for pressure which should be less than 10^{-10}. Two high order functions are utilized for interpolations, quadratic and cubic interpolations.

$$\frac{\partial U}{\partial t} + \frac{\partial F}{\partial x} + \frac{\partial G}{\partial y} = 0 \tag{1}$$

$$U = \begin{bmatrix} P \\ u \\ v \end{bmatrix} \quad F = \begin{bmatrix} \dfrac{u}{\beta} \\ u^2 + P - \dfrac{1}{Re}\dfrac{\partial u}{\partial x} \\ uv - \dfrac{1}{Re}\dfrac{\partial v}{\partial x} \end{bmatrix} \quad G = \begin{bmatrix} \dfrac{v}{\beta} \\ uv - \dfrac{1}{Re}\dfrac{\partial u}{\partial y} \\ v^2 + P - \dfrac{1}{Re}\dfrac{\partial v}{\partial y} \end{bmatrix} \tag{2}$$

1 General Validation

1.1 Correctness of residual

Second order centered fluxes are used to compute the flux integrals. The equation for flux integration on the right face of each cell is presented as Eqs. 3 and 4. Flux integration is carried out on a 1×1 square. This calculation is compared through L_2 norm of error of each term in the solution vector with an exact solution for the initial data presented in Eq. 5. The exact flux integral for this initial conditions is presented in Eq. 6. The variables in this equation are defined in Eq. 7. u_o, v_o, P_o, and β are all set to 1 with Re=10. The L_2

1

norm of error between these two solutions vs. mesh size is presented in Table 1. Further the ratio of errors and accuracy of the results are presented which show the second order accuracy of flux integration.

$$
F_{i+\frac{1}{2},j} =
\begin{bmatrix}
\dfrac{\overline{u}_{i+1,j} + \overline{u}_{i,j}}{2\beta} \\[2ex]
\left(\dfrac{\overline{u}_{i+1,j} + \overline{u}_{i,j}}{2}\right)^2 + \dfrac{\overline{P}_{i+1,j} + \overline{P}_{i,j}}{2} - \dfrac{1}{\mathrm{Re}}\dfrac{\overline{u}_{i+1,j} - \overline{u}_{i,j}}{\Delta x} \\[2ex]
\left(\dfrac{\overline{u}_{i+1,j} + \overline{u}_{i,j}}{2}\right)\left(\dfrac{\overline{v}_{i+1,j} + \overline{v}_{i,j}}{2}\right) - \dfrac{1}{\mathrm{Re}}\dfrac{\overline{v}_{i+1,j} - \overline{v}_{i,j}}{\Delta x}
\end{bmatrix}
\tag{3}
$$

$$
G_{i,j+\frac{1}{2}} =
\begin{bmatrix}
\dfrac{\overline{v}_{i,j+1} + \overline{v}_{i,j}}{2\beta} \\[2ex]
\left(\dfrac{\overline{u}_{i,j+1} + \overline{u}_{i,j}}{2}\right)\left(\dfrac{\overline{v}_{i,j+1} + \overline{v}_{i,j}}{2}\right) - \dfrac{1}{\mathrm{Re}}\dfrac{\overline{u}_{i,j+1} - \overline{u}_{i,j}}{\Delta y} \\[2ex]
\left(\dfrac{\overline{v}_{i,j+1} + \overline{v}_{i,j}}{2}\right)^2 + \dfrac{\overline{P}_{i,j+1} + \overline{P}_{i,j}}{2} - \dfrac{1}{\mathrm{Re}}\dfrac{\overline{v}_{i,j+1} - \overline{v}_{i,j}}{\Delta x}
\end{bmatrix}
\tag{4}
$$

$$
U =
\begin{bmatrix}
P_o \cos(\pi x)\cos(\pi y) \\
u_o \sin(\pi x)\sin(2\pi y) \\
v_o \sin(2\pi x)\sin(\pi y)
\end{bmatrix}
\tag{5}
$$

$$
-\frac{\partial F}{\partial x} - \frac{\partial G}{\partial y} =
\begin{bmatrix}
-\dfrac{\pi}{\beta}\left(u_o C_x S_{2y} + v_o S_{2x} C_y\right) \\[2ex]
P_o \pi S_x C_y - u_o^2 \pi S_{2x} S_{2y}^2 - u_o v_o \pi S_x S_{2x}(C_y S_{2y} + 2C_{2y} S_y) - u_o \dfrac{5\pi^2 S_x S_{2y}}{\mathrm{Re}} \\[2ex]
P_o \pi C_x S_y - V_o^2 \pi S_{2y} S_{2c}^2 - u_o v_o \pi S_y S_{2y}(C_x S_{2x} + 2C_{2x} S_x) - v_o \dfrac{5\pi^2 S_y S_{2x}}{\mathrm{Re}}
\end{bmatrix}
\tag{6}
$$

$$
\begin{cases}
C_x = \cos(\pi x) \\
S_x = \sin(\pi x) \\
C_y = \cos(\pi y) \\
S_y = \sin(\pi y) \\
C_{2x} = \cos(2\pi x) \\
S_{2x} = \sin(2\pi x) \\
C_{2y} = \cos(2\pi y) \\
S_{2y} = \sin(2\pi y)
\end{cases}
\tag{7}
$$

2

Table 1: Flux integration L$_2$ error with the exact flux.

Term	Mesh	Error	Ratio	Accuracy
R[0]	10x10	0.0479469		
	20x20	0.0119834	4.001110	2.000400
	40x40	0.0029957	4.000200	2.000072
	80x80	0.000748916	4.000048	2.000017
	160x160	0.000187228	4.000021	2.000008
	320x320	4.68E-05	3.999991	1.999997
R[1]	10x10	0.196283		
	20x20	0.0503244	3.900355	1.963605
	40x40	0.01266	3.975071	1.990981
	80x80	0.00316995	3.993754	1.997745
	160x160	0.000792797	3.998438	1.999437
	320x320	0.000198219	3.999601	1.999856
R[2]	10x10	0.200026		
	20x20	0.0512679	3.901584	1.964060
	40x40	0.0128964	3.975365	1.991087
	80x80	0.00322907	3.993843	1.997778
	160x160	0.000807578	3.998462	1.999445
	320x320	0.000201914	3.999614	1.999861

1.2 Correctness of implicit discretization flux Jacobian

The implicit time discretization of the Navier-Stokes equations can be written as follows.

$$
\begin{aligned}
&\delta U_{i,j} + \Delta t A_x \delta U_{i-1,j} + \Delta t B_x \delta U_{i,j} + \Delta t C_x \delta U_{i+1,j} \\
&+ \Delta t A_y \delta U_{i,j-1} + \Delta t B_y \delta U_{i,j} + \Delta t C_y \delta U_{i,j+1} = \\
&- \Delta t \frac{F^n_{i+\frac{1}{2},j} - F^n_{i-\frac{1}{2},j}}{\Delta x} - \Delta t \frac{G^n_{i,j+\frac{1}{2}} - G^n_{i,j-\frac{1}{2}}}{\Delta y}
\end{aligned}
\tag{8}
$$

The left hand side of this equation arises from the following approximation.

$$
\begin{aligned}
&\left(\frac{F_{i+\frac{1}{2},j} - F_{i-\frac{1}{2},j}}{\Delta x} + \frac{G_{i,j+\frac{1}{2}} - G_{i,j-\frac{1}{2}}}{\Delta y} \right)^{n+1} \\
&- \left(\frac{F_{i+\frac{1}{2},j} - F_{i-\frac{1}{2},j}}{\Delta x} + \frac{G_{i,j+\frac{1}{2}} - G_{i,j-\frac{1}{2}}}{\Delta y} \right)^{n} \approx \\
&A_x \delta U_{i-1,j} + B_x \delta U_{i,j} + C_x \delta U_{i+1,j} + A_y \delta U_{i,j-1} + B_y \delta U_{i,j} + C_y \delta U_{i,j+1}
\end{aligned}
\tag{9}
$$

The correctness of the right hand side of this equation is proved in the previous section. I will calculate residual for the data set presented in the previous section

and then update the solution vector with the following differential change.

$$
\delta U_{i,j} = \begin{cases} 10^{-6} \begin{bmatrix} 1 \\ 1 \\ 1 \end{bmatrix} & i,j = 10 \\ \\ 0 & i/j \neq 10 \end{cases}
\tag{10}
$$

The new residual is calculated and with that the left hand side of Eq. 9 is computed. This calculation is conducted on a 20×20 mesh and the error for each term is presented in Table 2.

Table 2: Implicit discretization flux Jacobian calculation L_2 error.

Term	Error
[0]	2.88E-17
[1]	5.00E-13
[2]	5.00E-13

3 Flow in a Box with a Moving Top

The famous cavity problem is selected for code validation. The walls have no-slip boundary conditions with the top wall moving at a constant velocity. The fluid is isothermal which means no buoyancy effects. Reynolds number is set to 100 with $\beta = 1.0$. A schematic view of this problem is presented in Fig. 1.

3.1 Validation case

The initial condition of previous sections is used here as well. Setting $U_{\text{top}} = 0.0$ and $h = 1.0$ we should get zero velocity at the steady state solution and a constant pressure everywhere. The solution is carried out and the average value and standard deviation from average of each term is calculated in the domain. These results are presented in Table 3. As seen in this table, the average velocity components are very close to zero with small standard deviation. Also, pressure has a non-zero constant value with a small standard deviation. The value of pressure is negative only for the 40×40 mesh, which is strange. The convergence history of this simulation with $\Delta t = 0.05$ and $\beta = 1.0$ is plotted for all three terms in the solution vector. Figs. 2, 3, and 4 show the error between consecutive solutions (up to 200 iterations) on grids of 10×10, 20×20, and 40×40, respectively. The convergence L_2 norm of error is oscillatory because of the oscillations of pressure in the solution domain. These oscillations are errors propagating in the solution domain, hitting the boundaries and coming back for another pass. The frequency of oscillations is somewhat constant. The period of each oscillation in the convergence history plot should be about $\frac{1.0}{\Delta t}$ which in this case is equal to 20. And yes, the oscillations have a period of about 20
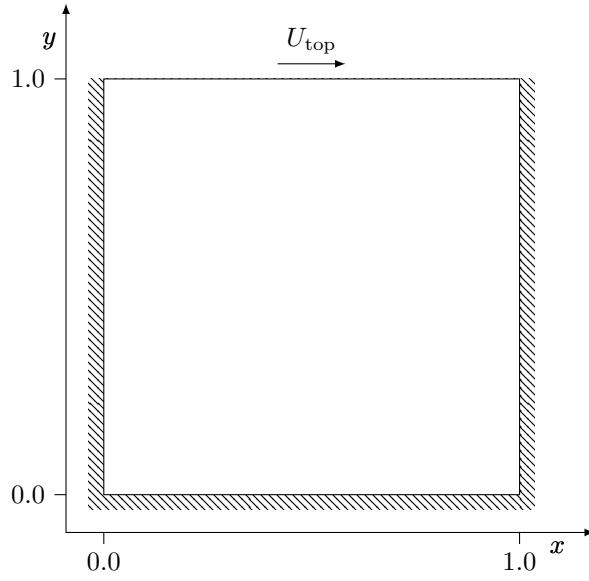
Figure 1: The physical domain of solution.

iterations in these plots. However, the same analysis did not work for other time steps. This frequency is a function of Δt, mesh size, β, and Reynolds number, I think.

Table 3: Steady state solution average and standard deviation for $U_{\text{top}} = 0.0$.

Mesh	P mean	P SD	u mean	u SD	v mean	v SD
10x10	0.00205829	3.71E-09	-2.64E-10	4.77E-10	2.98E-10	4.12E-10
20x20	0.0062983	1.86E-09	-4.63E-10	3.73E-10	1.71E-10	2.03E-10
40x40	-0.00225158	1.31E-08	1.91E-11	6.01E-10	3.51E-12	1.46E-10
80x80	0.00015934	5.23E-08	-1.06E-11	6.26E-10	-1.73E-12	1.06E-10
160x160	0.000251319	2.08E-07	-3.31E-15	3.47E-12	-5.51E-12	6.37E-10
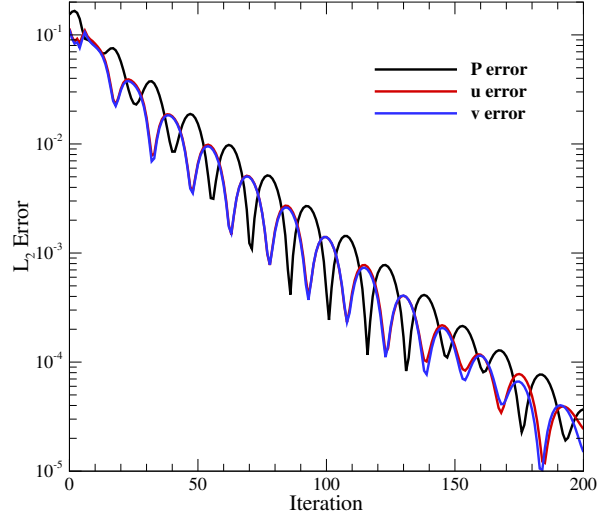
Figure 2: Convergence history of solution with $U_{\text{top}} = 0.0$ on a 10×10 mesh.
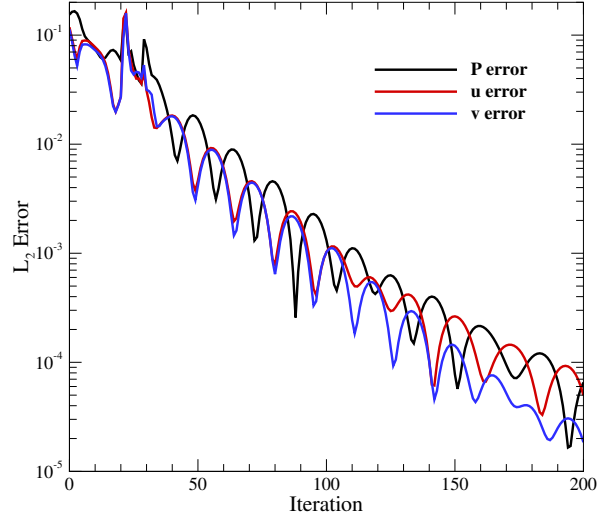
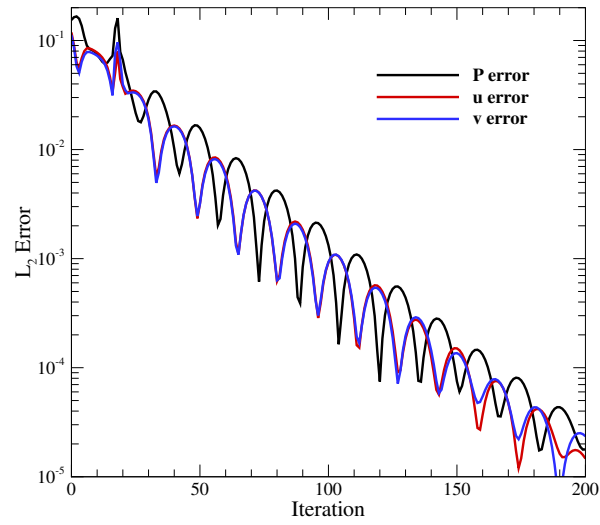Figure 3: Convergence history of solution with $U_{\text{top}} = 0.0$ on a 20×20 mesh.

6

Figure 4: Convergence history of solution with $U_{\text{top}} = 0.0$ on a 40×40 mesh.

3.2 Solution for $U_{\mathbf{top}} = 1.0$

A 20×20 mesh is used with $U_{\text{top}} = 1.0$ and Re=100 in this section. The contour of pressure of the solution is presented in Fig. 5 while Fig. 6 shows the streamlines. As seen in Fig. 5, pressure is highest at the top right corner and lowest at top left corner. Further, the distribution of u along $x = 0.5$ and distribution of v along $y = 0.5$ are presented in Fig. 7. This figure also compares the results of the present study to the results of Ghia in [1]. As seen here, the results are very similar. Convergence history of this test is presented in Fig. 8. Δt is set to 0.5 for this solution.
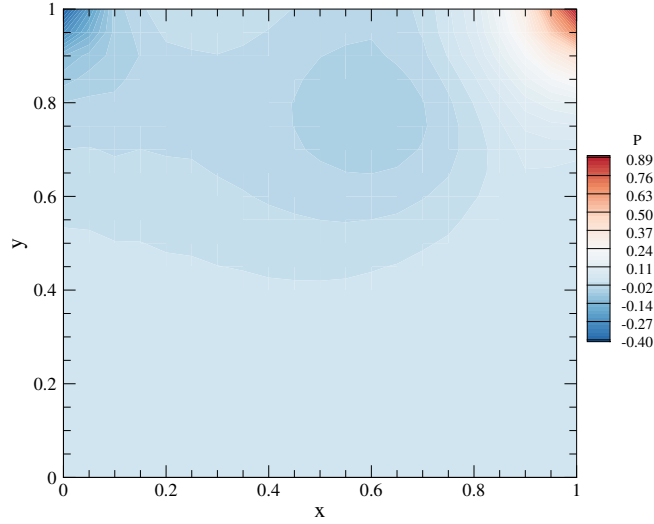
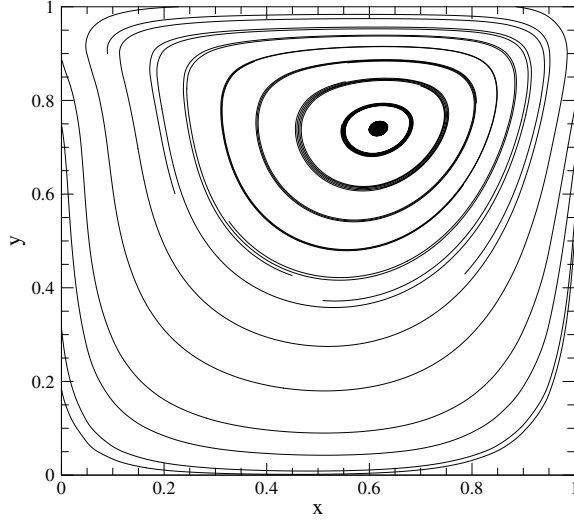Figure 5: Pressure contours with $U_{\text{top}} = 1.0$ and Re=100 on a 20×20 mesh.

8

Figure 6: Streamlines with $U_{\text{top}} = 1.0$ and Re=100 on a 20×20 mesh.
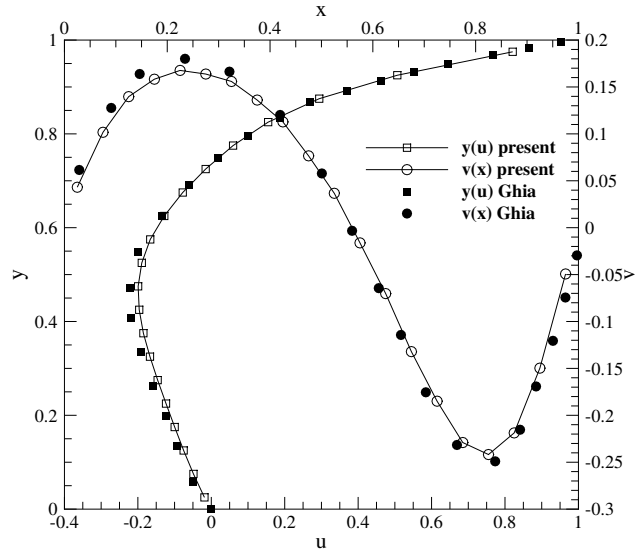

Figure 7: Distribution of u along $x = 0.5$ and v along $y = 0.5$ for Re=100.
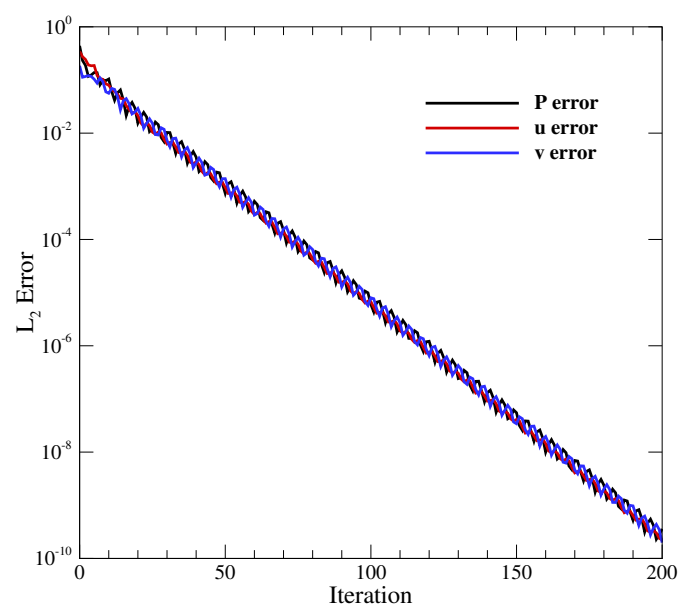
9

Figure 8: Convergence history for Re=100 on a 20×20 mesh.

10

3.3 Sanity check

The exact same problem of the previous section is solved again with $U_{\text{top}} = -1.0$. The contour of horizontal velocity for $u_{U_{\text{top}}=1.0}(x,y) + u_{U_{\text{top}}=-1.0}(1-x,y)$ is plotted in Fig. 9. As seen here, the difference between the two solutions is very small everywhere with a maximum of less than 10^{-8}. The average value in this plot is 1.9750×10^{-11} with a standard deviation of 1.1201×10^{-9}.
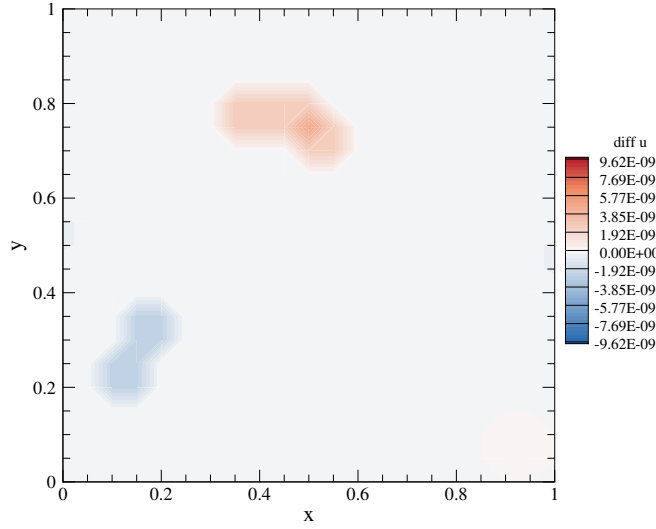

Figure 9: Contour of $u_{U_{\text{top}}=1.0}(x,y) + u_{U_{\text{top}}=-1.0}(1-x,y)$.

3.4 Grid convergence

The solution is carried out for $U_{\text{top}} = 1.0$ on different mesh sizes to study the grid convergence. A cubic interpolation is utilized to find the velocity at the desired location. The horizontal velocity distribution along $x = 0.5$ is presented on all the meshes in Fig. 10. A closer view of this solution is presented in Fig. 11. As seen, the solutions on meshes larger than 80×80 are almost identical. The distribution of v on $y = 0.5$ is presented in Fig. 12 which confirms solution accuracy and grid convergence on the 80×80 mesh. Grid convergence of solution data (according to [2]) is carried out for the horizontal component of velocity at the center of the domain $(x,y) = (0.5, 0.5)$. The results are presented in Table 4. According to this table grid convergence index is very close to zero at fine meshes which indicates convergence, obviously. Further, the order of accuracy is close to 2 which is what we were looking for. Grid convergence index of meshes finer than 80×80 is less than 1 percent and I think this mesh is the coarsest
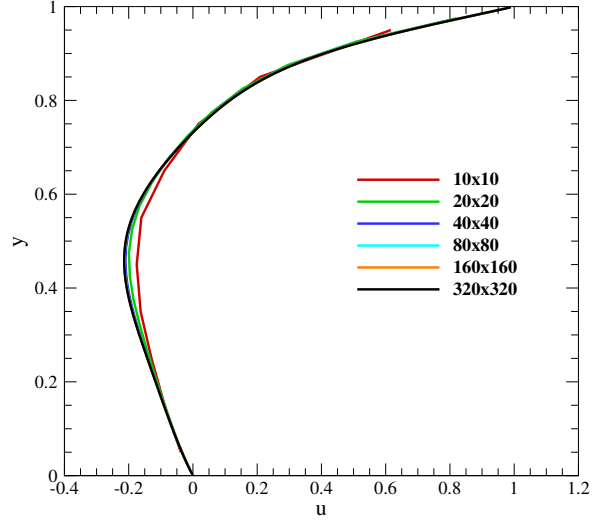
we need for grid convergence.

Figure 10: Distribution of u along $x = 0.5$ for different mesh sizes.

Table 4: Grid convergence study for u at $(x, y) = (0.5, 0.5)$.

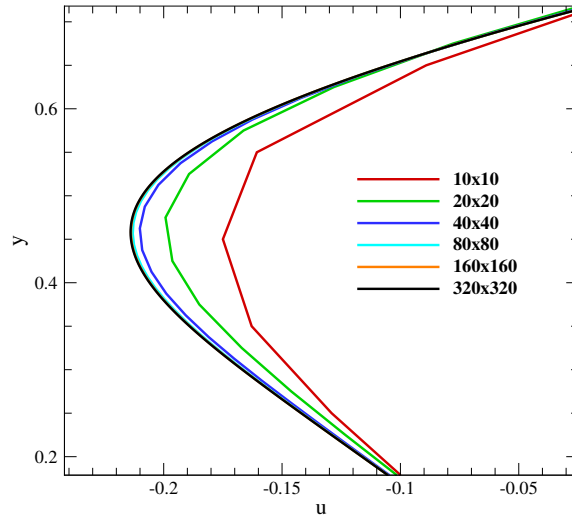| Mesh	u	Difference	Apparent Order	Rel. Error [%]	Extrap. Value	GCI [%]
10×10	-0.173051					
20×20	-0.19588	0.022829		13.192065		
40×40	-0.205559	0.009679	1.237938	4.941291	-0.212683	4.546269
80×80	-0.208244	0.002685	1.849936	1.306194	-0.209275	0.626811
160×160	-0.208924	0.00068	1.981315	0.326540	-0.209155	0.138433
320×320	-0.209093	0.000169	2.008511	0.080891	-0.209149	0.033441

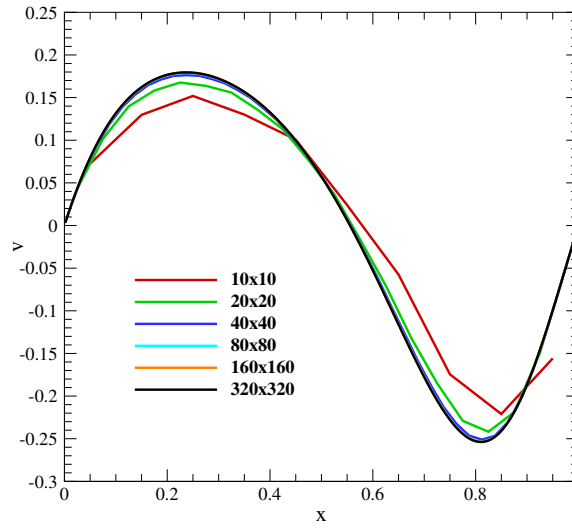Figure 11: Distribution of u along $x = 0.5$ for different mesh sizes.

Figure 12: Distribution of v along $y = 0.5$ for different mesh sizes.

13

4 Effect of Increasing h

As the ratio of height to width of the box increases, the single vortex eventually becomes unstable, and a second vortex forms below it. There can be even more vortices if this ratio is sufficiently large. The convergence criteria on u is the L_2 norm of error which should be less than 10^{-10}. For this part, Re is set to 300 with $U_{\text{top}} = 1.0$, $w = 1$, and $h = 2.5$. β is reduced to get a faster convergence rate. We have to be careful about the time step as it has a considerable effect on the stability of the numerical solution. The pressure contours and streamlines on a 80×200 mesh are presented in Figs. 13 and 14, respectively. The magnitude of u on $x = 0.5$ is presented in Fig. 15. The convergence history for this test is presented in Fig. 16. As seen in this figure, pressure is oscillating until about 3000 iterations and after that the oscillations in pressure attenuates. This might be due to the very small changes in the solution after that point which until then were a cause for pressure oscillations. Furthermore, I have utilized first order boundary conditions for a second order discretization of the solution domain. This means that errors will attenuate after each time hitting the boundaries. Also, pressure is converging faster than the two components of velocity. u is converging faster than v as well.

In this simulation two primary vortices are formed. However, there are smaller secondary vortices on the bottom corners of the domain (just like the previos sections). The center of a vortex is a place where velocity goes to zero. We have to use a high order interpolation (or integration for that matter) to find the center of each primary vortex. I have used a high order integration method to get the convergence point of the streamlines. In this method a random point is chosen and then velocities are interpolated over this point with a cubic interpolation. Then streamlines are integrated moving forward from the initial point until a single point is found for the center location. The center point of the two primary vortices on a 160×400 mesh are presented in Table 5. Grid convergence of solution data (according to [2]) is carried out for the location of each vortex. The results are presented in Tables 6, 7, 8, and 9. According to these tables, grid convergence index is very close to zero at fine meshes which indicates convergence, obviously. Further, the order of accuracy is close to 2 which is what we were looking for. The results of the 10×25 mesh are not that convincing due to lack of numerical resolution.

In a steady state condition, the mass flow rate integral over a horizontal line through the primary vortex center should be zero. Which means whatever amount of mass flow rate is on the right side of the center location is equal to the mass flow rate on the left side (only with different sign). In fact, mass flow rate is a very good estimate of the vortex strength. As a result, I have integrated the mass flow rate over horizontal lines connecting the primary vortex centers to the side walls. These integration lines are depicted in Fig. 17. These results are nondimensionalized with the distance from wall $(\frac{\dot{m}}{\text{distance}})$ simply refered to as mass flow rate or $\dot{m}$ here. Velocity interpolation is carried out with a quadratic interpolation function (using 3 points every time). These results are presented in Table 10 for different mesh sizes. As seen in this table, the net value of mass

flow rate on a horizontal line going through the center of each vortex goes to zero with mesh size which is a sign of grid convergence. Also, this definition of vortex strength is almost constant with changes in grid size. Grid convergence calculation is carried out for the vortex mass flow rate. The results are presented in Tables 11, 12, 13, and 14. According to these tables, grid convergence index is very close to zero at fine meshes which indicates convergence. Further, the order of accuracy is close to 2 which is what we were looking for.
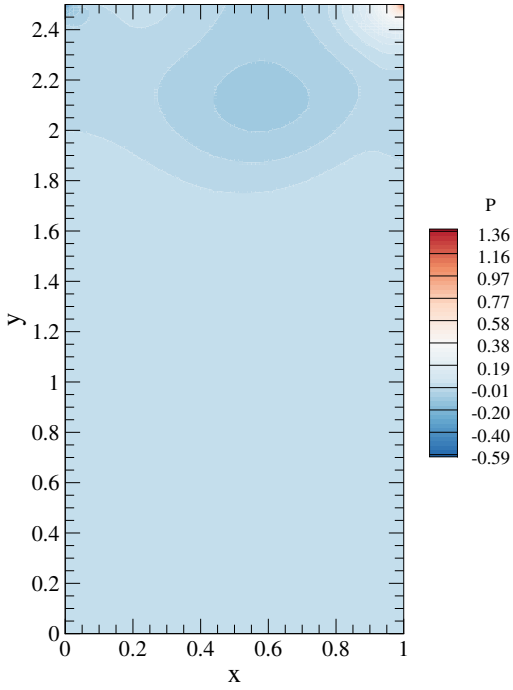

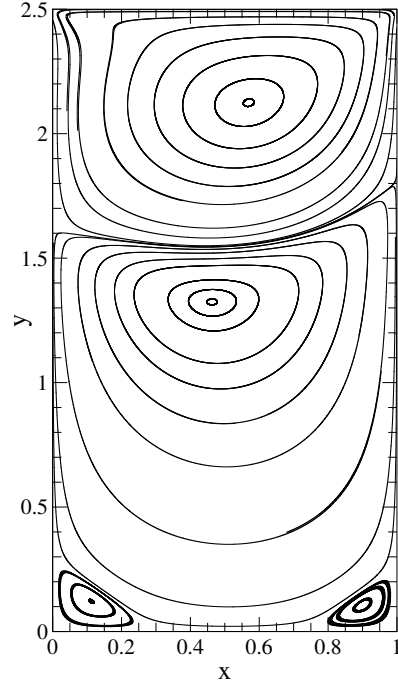Figure 13: Pressure contours on a 80×200 mesh.

Figure 14: Streamlines on a 80×200 mesh.

Table 5: Center location of the two primary vortices.

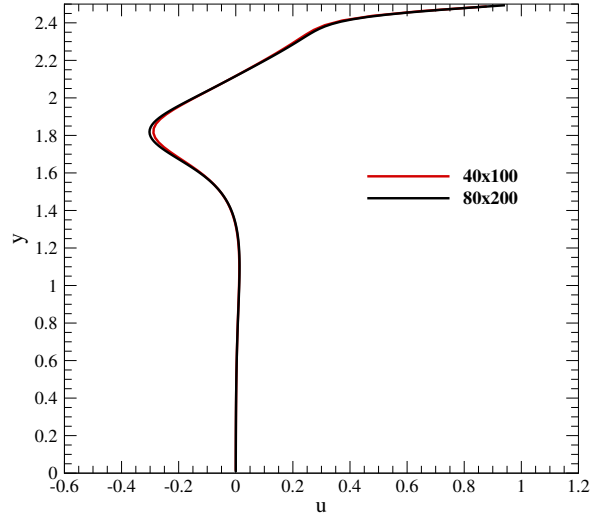| Vortex	x location	y location
Top	0.56843	2.12379
Bottom	0.461183	1.32682

15

Figure 15: Distribution of u along $x = 0.5$ for different mesh sizes.
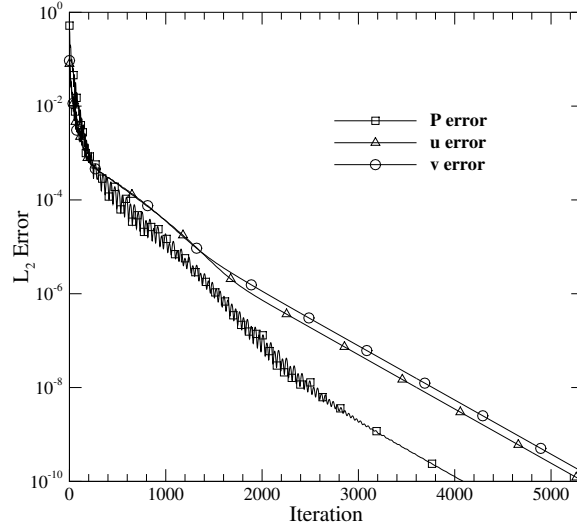

Figure 16: Convergence history on a 80×200 mesh.

16

Table 6: Grid convergence study for x location of the primary top vortex.

Mesh	x location	Difference	Apparent Order	Rel. Error [%]	Extrap. Value	GCI [%]
10x25	0.614291					
20x50	0.590038	0.024253		3.948129		
40x100	0.57311	0.016928	0.518752	2.868968	0.533990	8.287694
80x200	0.569345	0.003765	2.168690	0.656942	0.568268	0.234881
160x400	0.56843	0.000915	2.040806	0.160711	0.568136	0.064496

Table 7: Grid convergence study for y location of the primary top vortex.

Mesh	y location	Difference	Apparent Order	Rel. Error [%]	Extrap. Value	GCI [%]
10x25	2.07453					
20x50	2.13287	-0.058340		2.812203		
40x100	2.12583	0.007040	3.050838	0.330072	2.124864	0.056620
80x200	2.12407	0.001760	2.000000	0.082791	2.123483	0.034496
160x400	2.12379	0.000280	2.652077	0.013182	2.123737	0.003117

Table 8: Grid convergence study for x location of the primary bottom vortex.

Mesh	x location	Difference	Apparent Order	Rel. Error [%]	Extrap. Value	GCI [%]
10x25	0.535204					
20x50	0.491325	0.043879		8.198556		
40x100	0.469814	0.021511	1.028456	4.378161	0.449127	5.263022
80x200	0.462923	0.006891	1.642289	1.466751	0.459675	0.864174
160x400	0.461183	0.001740	1.985626	0.375872	0.460595	0.158711

Table 9: Grid convergence study for y location of the primary bottom vortex.

Mesh	y location	Difference	Apparent Order	Rel. Error [%]	Extrap. Value	GCI [%]
10x25	0.924126					
20x50	1.28507	-0.360944		39.057877		
40x100	1.31565	-0.030580	3.561115	2.379637	1.318481	0.275338
80x200	1.32439	-0.008740	1.806883	0.664310	1.327888	0.332307
160x400	1.32682	-0.002430	1.846677	0.183481	1.327756	0.088324

Table 10: Nondimensionalized mass flow rate over left and right horizontal lines of primary vortices.

Primary Vortex	Mesh	Left Hor. Line $\dot{m}$	Right Hor. Line $\dot{m}$	Net
	10x25	0.150482	-0.152757	-2.2750E-03
	20x50	0.17479	-0.175245	-4.5500E-04
Top	40x100	0.190585	-0.190559	2.6000E-05
	80x200	0.195634	-0.195637	-3.0000E-06
	160x400	0.1969829	-0.196983	-1.0000E-07
	10x25	-0.00370997	0.00128356	-2.4264E-03
	20x50	-0.0110813	0.0106	-4.8130E-04
Bottom	40x100	-0.0142077	0.0142594	5.1700E-05
	80x200	-0.0152906	0.0152818	-8.8000E-06
	160x400	-0.0155516	0.0155502	-1.4000E-06

Table 11: Grid convergence study for mass flow rate on the left hand side of the primary top vortex.

Mesh	$\dot{m}$	Difference	Apparent Order	Rel. Error [%]	Extrap. Value	GCI [%]
10x25	0.150482					
20x50	0.17479	-0.024308		16.153427		
40x100	0.190585	-0.015795	0.621963	9.036558	0.219891	20.958011
80x200	0.195634	-0.005049	1.645398	2.649212	0.198006	1.555913
160x400	0.19698299	-0.001349	1.904118	0.689548	0.197475	0.314254

Table 12: Grid convergence study for mass flow rate on the right hand side of the primary top vortex.

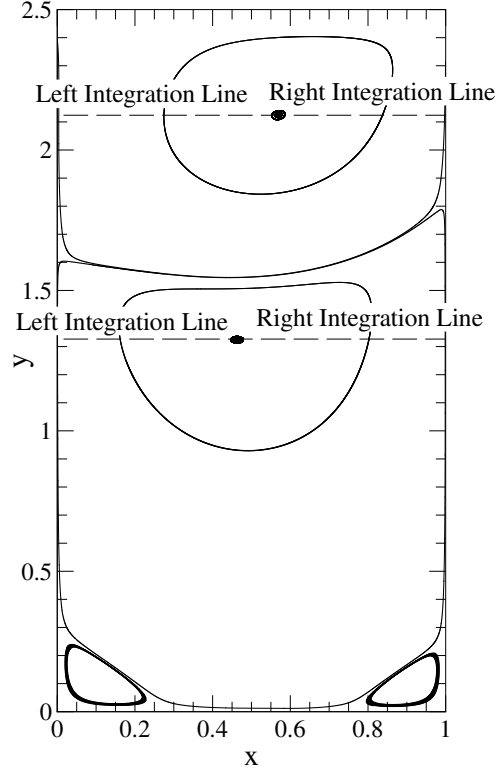| Mesh	$\dot{m}$	Difference	Apparent Order	Rel. Error [%]	Extrap. Value	GCI [%]
10x25	-0.152757					
20x50	-0.175245	0.022488		14.721420		
40x100	-0.190559	0.015314	0.554304	8.738623	-0.223249	23.317409
80x200	-0.195637	0.005078	1.592519	2.664791	-0.198156	1.652478
160x400	-0.19698301	0.001346	1.915571	0.688014	-0.197468	0.310181

Figure 17: Integration lines for mass flow rate.

Table 13: Grid convergence study for mass flow rate on the left hand side of the primary bottom vortex.

Mesh	$\dot{m}$	Difference	Apparent Order	Rel. Error [%]	Extrap. Value	GCI [%]
10x25	-0.00370997					
20x50	-0.0110813	0.007371		198.689747		
40x100	-0.0142077	0.003126	1.237423	28.213296	-0.016510	25.973941
80x200	-0.0152906	0.001083	1.529602	7.621923	-0.015864	5.048802
160x400	-0.0155516	0.000261	2.052778	1.706931	-0.015634	0.677560

Table 14: Grid convergence study for mass flow rate on the right hand side of the primary bottom vortex.

Mesh	$\dot{m}$	Difference	Apparent Order	Rel. Error [%]	Extrap. Value	GCI [%]
10x25	0.00128356					
20x50	0.0106	-0.009316		725.828165		
40x100	0.0142594	-0.003659	1.348172	34.522642	0.016627	27.914809
80x200	0.0152818	-0.001022	1.839647	7.170007	0.015678	3.474884
160x400	0.0155502	-0.000268	1.929503	1.756338	0.015646	0.781500

5 Complementary Results

5.1 Effect of Reynolds number

A numerical grid of 160×160 is used for the calculations in this section. The numerical solution is carried out and the results are presented. Figs. 18 and 19 show the streamlines for solutions with Reynolds numbers of 1000 and 5000, respectively. At Re=5000 a new secondary vortex emerges from the top left corner of the domain. Also, a small vortex forms beneath the bottom right corner secondary vortex. Figs. 20 and 21 show u and v on the symmetry lines of the domain for Reynolds numbers of 1000 and 5000, respectively. These results are also compared to the data from [1]. As seen, there are good agreement between the results which show the accuracy of the simulations.
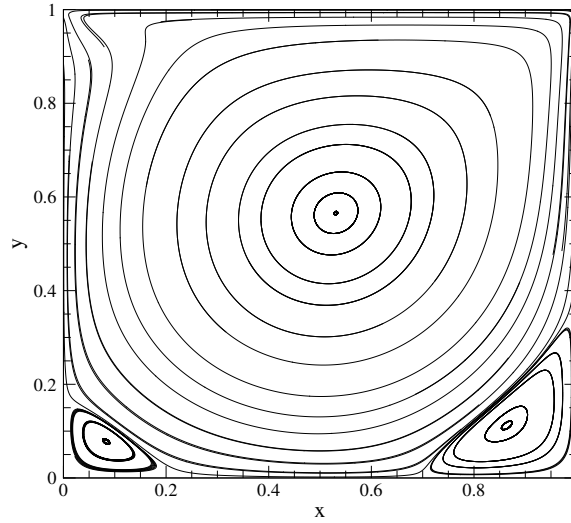
Figure 18: Streamlines in the solution with Re=1000.
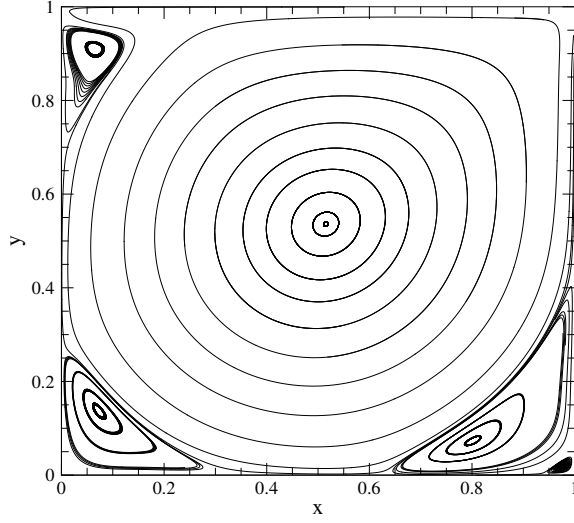
Figure 19: Streamlines in the solution with Re=5000.
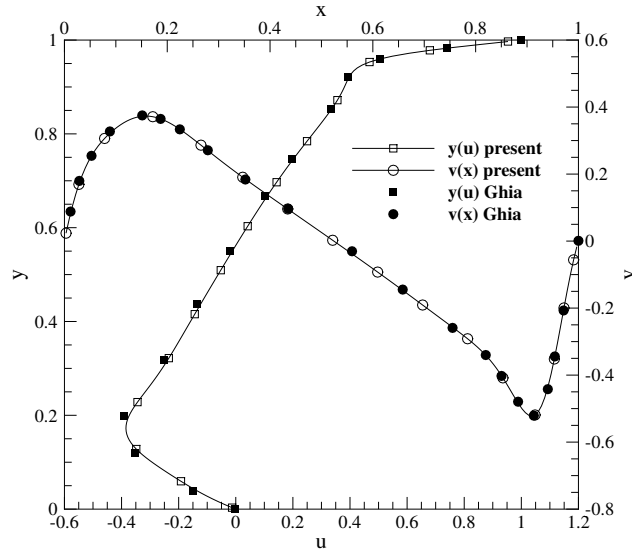
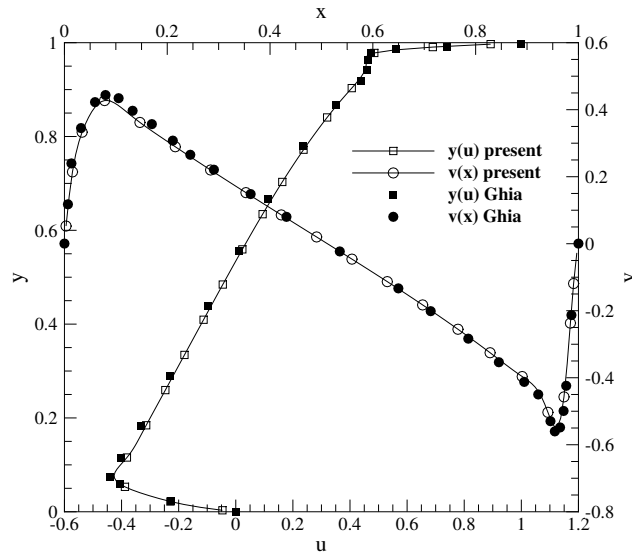Figure 20: u and v distribution on symmetry lines of the domain at Re=1000.

Figure 21: u and v distribution on symmetry lines of the domain at Re=5000.

5.2 Effect of β

A 40×40 mesh is selected with Re=100 on the rectangular domain for this section. The convergence history is plotted in Fig. 22 for different values of β. The fastest convergence history belongs to $\beta = 0.1$ with only 400 iterations to full convergence to 10^{-10}. On the other hand, $\beta = 2.0$ and $\beta = 0.02$ are the worst performers.
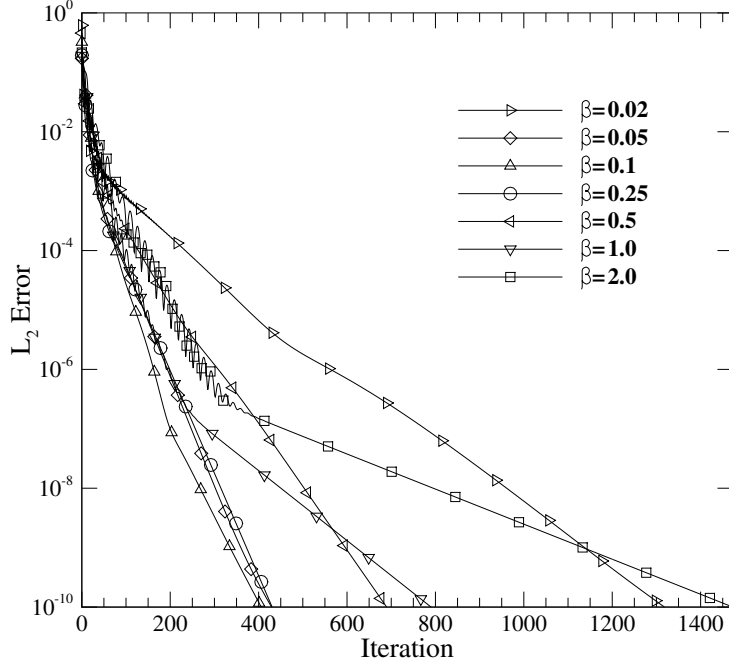
Figure 22: Convergence history on a 40×40 mesh with different values of β.

5.3 Effect of h/w

A Reynolds number of 300 is used for the present section. Changing $\frac{h}{w}$ has interesting effects on the behavior and the number of vortices present in the flow. Figs. 23, 24, 25, and 26 show the streamlines for $\frac{h}{w} = 2$, 3, 4, and 5, respectively. These contours are rotated clockwise to get the most out of paper real estate. It is important to mention that adjacent vortices in this problem are counter rotating. Increasing $\frac{h}{w}$ at constant Re, results in increasing number of vortices. Further, these vortices might be unstable in reality. We are conducting a steady state solution which makes any unstable feature in the

domain to vanish. I think a better analysis here should be carried out with an unsteady Navier-Stokes solver.
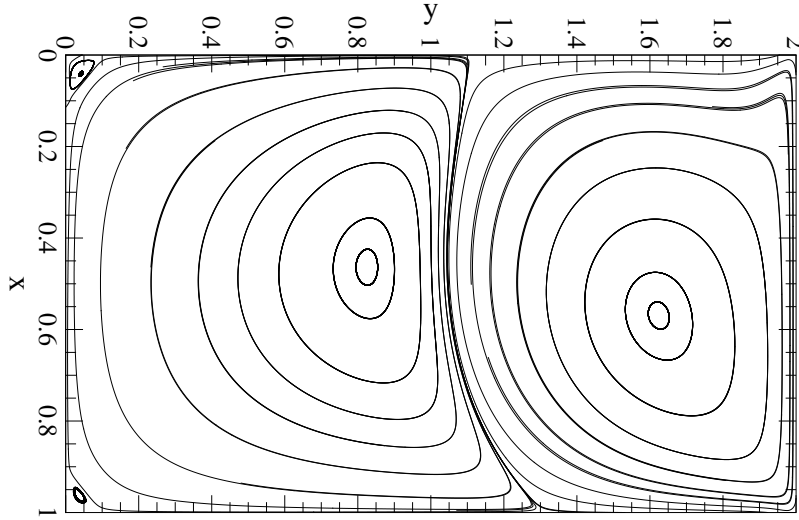

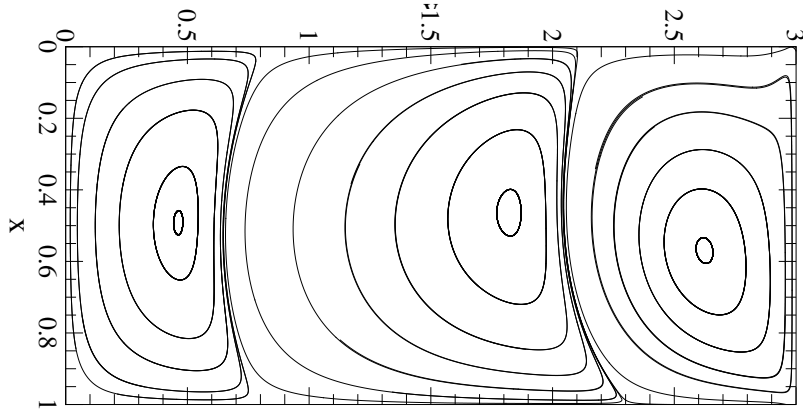Figure 23: Stream lines in the solution with Re=300 and $\frac{h}{w} = 2$.

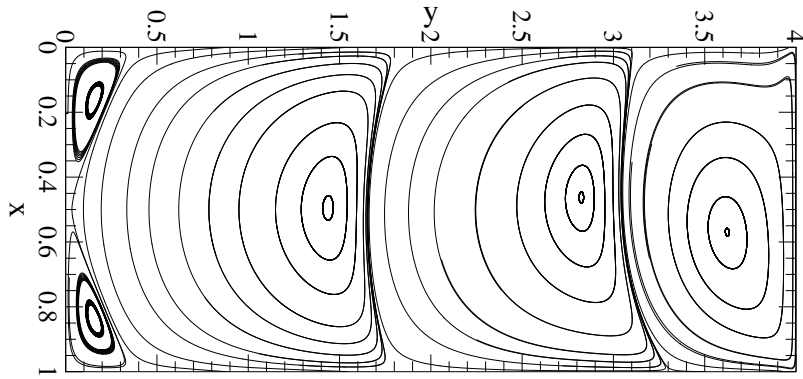Figure 24: Stream lines in the solution with Re=300 and $\frac{h}{w} = 3$.

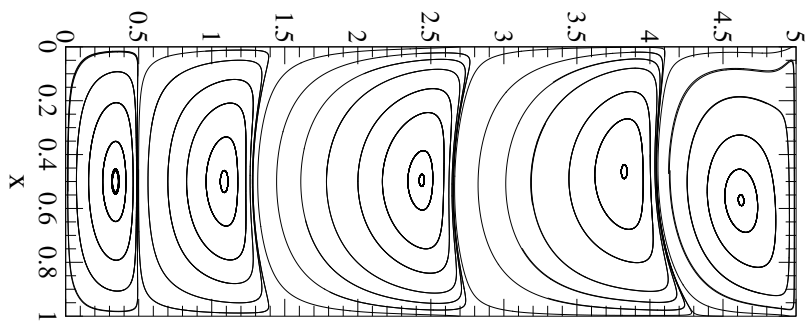Figure 25: Stream lines in the solution with Re=300 and $\frac{h}{w} = 4$.

26

Figure 26: Stream lines in the solution with Re=300 and $\frac{h}{w} = 5$.

References

[1] U Ghia, K.N Ghia, and C.T Shin. High-re solutions for incompressible flow using the navier-stokes equations and a multigrid method. *Journal of Computational Physics*, 48(3):387 – 411, 1982.

[2] Procedure for Estimation and Reporting of Uncertainty Due to Discretization in CFD Applications. *Journal of Fluids Engineering*, 130(7), 07 2008.